Progress In Electromagnetics Research, PIER 96, 63–82, 2009

WIENER FILTERING APPLIED TO MAGNETIC NEAR FIELD SCANNING

C. Labarre †

Université Lille Nord de France
Lille F 59000, France

F. Costa and C. Gautier ‡

SATIE (UMR 8029)
ENS de Cachan PRES UniverSud
61 av. du président Wilson, Cachan 94235, France

Abstract—Magnetic near-field scanning is a growing-up technique in power electronics. However, due to the large size of the devices, a trade-off is necessary to find between the spatial resolution of the field and the measurement time, this one is often unsatisfying. In this paper, we propose to improve drastically this trade-off by using a signal-processing technique (Wiener filtering) which allows a large scanning step (short scanning duration) while keeping an accurate spatial resolution of the magnetic field. This technique is adapted to the magnetic near-field probing, as described in the paper. Our experiments show that a factor 25 can be gained on the product "resolution-×-duration" of the measurements.

1. INTRODUCTION

Measurement techniques that are usually used for the characterization of radiated and conducted emissions of power electronics are mainly concerned by the compliance with EMC standards. Actually, near field techniques constitute also an efficient approach to characterize complex radiating systems; they have been successfully applied in the microwave

---

Corresponding author: C. Labarre (labarre@ensm-douai.fr).

† C. Labarre is also with EM Douai, IA, Douai F 59508, France.

‡ F. Costa is also with IUFM de Créteil, Université Paris 12, place du 8 mai 1945, Saint-Denis 93000, France; C. Gautier is also with Université Paris 10, IUT de Ville d'Avray, 1 chem. Desvallières, Ville d'Avray 92410, France.

domain [1, 2]. However, near field scanning over a power electronic device is not referenced in standards, but it can be useful to estimate the characteristics of radiations and to locate spatially the sources of electromagnetic fields [11]. It can also be used to identify the couplings on sensitive components (filters, drives, sensors) and their propagation mode. This practice is growing up in power electronics [3]. Moreover, calculation techniques exist that allow calculating far field from "near field" measurements [12]. These methods can be useful for comparing emissions to standards limits without large measuring equipments. Ideally, the near field measurements should be punctual, but that is not possible due to the size of the probe. In fact, the probe integrates the field over an area depending on its size. Consequently, the user is balanced between the choice of a large probe having a good sensitivity but a poor spatial resolution and a small probe having the inverse performances. Our purpose is to develop a measurement technique based on signal processing which will conciliate the sensitivity of a large probe and the accuracy of a small one. This technique is based on the taking into account of the probe integration. In a first part, we describe briefly the test bench developed by our laboratory to measure the near magnetic field. We underline the trade-off between the probe size, its sensitivity and its resolution [4, 5]. In a second part, we have chosen to favour the sensitivity and to enhance the resolution by a signal processing technique, the Wiener filtering [6]. In a third part, we express the transfer function of the probe by three different methods and we check our technique on an industrial power electronic component.

2. NEAR-FIELD MEASUREMENT SYSTEM

2.1. Test Bench

A three-dimensional near-field scanner is used to measure the magnitude of the magnetic near-field in a plane at a fixed frequency above a power electronics device (Figure 1). The equipment is rated to work in a bandwidth situated between 9 kHz and 1 GHz but, as our applications are in the power electronics domain, our studied frequency range is reduced to 10 kHz–30 MHz. The loop-probe is connected to an EMI receiver; it is mounted on a displacement table. A computer monitors the probe displacement (along x and y) over the device under test (DUT) and it records data provided by the EMI receiver. The maximum scanning area is 500 mm × 500 mm × 500 mm; only the z-axis is manually actuated. The mechanical resolution is 0.1 mm in the two directions (x and y). A copper ground plane has been inserted in our system, in order to reproduce the effect of the heat-sink included in

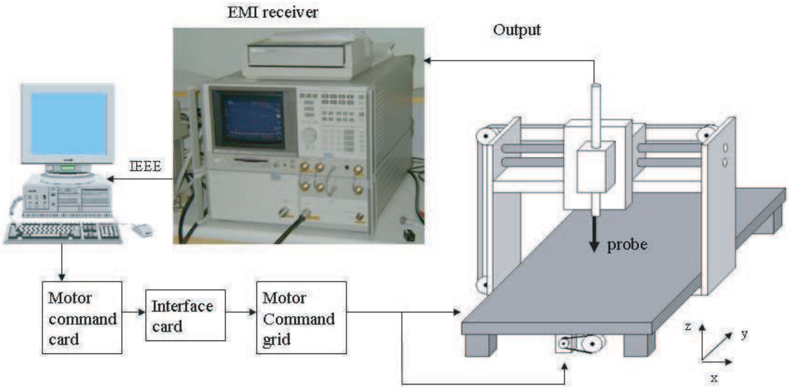

Figure 1. Near field hardware system.

Figure 2. Measurement setup.

many power electronic devices. All the displacements devices (motors, driving equipments), which are likely to induce electromagnetic field reflections, are located under this ground plane to prevent external perturbations. All the structural parts, which stand above this area, are made of unreflecting materials (Plexiglas, nylon). Figure 2 is a photograph of the test bench, the EMI receiver and driving computer.

The measurements of the three components of the magnetic field are achieved with H field probes (AFJ near-field probe, set LF1). Their frequency ranges are 100 kHz–50 MHz or 30 MHz–3 GHz. They consist of small electrically balanced loop antennas. These loop probes are built with an electric field shield and with a small break at one point. The gap in the shield prevents shield currents from flowing around the loop yet still permits electric field shielding of the center conductor as shown in Figure 3, in order to reduce the loop antenna's electric field response. Figure 4 is a picture of the two magnetic field probes used in this paper: The RF-R 400-1 which has a large diameter (25 mm) and the LF-R-3 which has a smaller diameter (3 mm). These loop probes measure the magnetic field perpendicular to the loop at a fixed frequency. The three components of the magnetic field are obtained by rotating the probe with an angle of 90° around the three x, y and z directions.

The voltage e induced at the open-ends of the probe is expressed by:

$$e = -\frac{d\phi}{dt} = -\frac{d}{dt}\left(\iint_{(S)} \overrightarrow{B} \bullet \overrightarrow{dS}\right) \tag{1}$$

S is the probe area.

By considering the magnetic field constant over the probe area, the magnetic field is linked to the measured voltage for an harmonic signal by:

$$e = -j\omega B \iint \overrightarrow{dS} = -j\omega\mu_0 H\, S \tag{2}$$

In its logarithmic form, the measured magnetic field is expressed by:

$$H_{dB} = V_{dB} + AF_{dB} + L_{dB} \tag{3}$$

where H_{dB} is the magnetic field in dBμA/m, V_{dB} is the voltage in dBμV measured by the EMI receiver, AF_{dB} is the probe performance

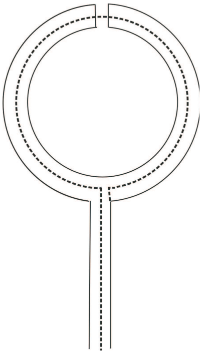

Figure 3. Shielded loop antenna.

Figure 4. The used near field probes.

factor in dB((μA/m)/μV) and L_{dB} is the cable losses between the probe and the EMI receiver.

2.2. Size, Resolution and Sensitivity of the Probe

Ideally this probe should simultaneously exhibit an excellent resolution, a high sensitivity and it should not disturb the field being measured. A smaller probe will introduce less disturbance in the field components being measured and will have a good spatial resolution but a low sensitivity. Indeed, if we consider a shielded probe, the electric component of the electromagnetic field induces a voltage on the shielding which doesn't affect the H-field measurement. The equivalent circuit of a small electrically balanced loop antenna (diameter $\ll \lambda$, wavelength) is represented in Figure 5.

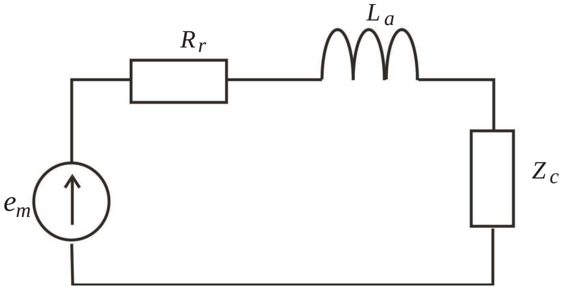

Figure 5. Equivalent circuit for an electrically small loop antenna.

e_m is the voltage induced by the H-field, R_r is the loop resistance, L_a is the loop inductance and Z_c is the load impedance (the EMI receiver input impedance Z_c is equal to $50\,\Omega$). In our studied frequency range (10 kHz–100 MHz), the loop impedance has been measured and is much smaller than Z_c, so the magnetic field probe provides an output voltage proportional to the magnetic field.

$$e_m = -j2\pi f \mu_0 H A \tag{4}$$

A is the loop area, f is the measurement frequency and μ_0 is the vacuum permeability.

The spectral sensitivity is defined by the ratio:

$$\left|\frac{e_m}{\mu_0 H f}\right| = \pi^2 \frac{D^2}{2} \tag{5}$$

The sensitivity increases as the loop size. So, the loop must be large enough to provide an adequate signal to noise ratio.

Smaller loops have obviously higher spatial resolution. An important source of error is due to the assumption that the probe voltage is related only to the field strength of a single point of space. Such a simplification is acceptable only for devices that produce field patterns with smooth changes in a spatial range greater than the probe size. However, the use of such a method for the measurement of the near-field within a spatial distribution that rapidly changes produces a blurring effect caused by the integration of the nearby fields due to the finite size of the probe. This problem can be solved by decreasing the spatial step of the measurements (about 1 mm) but this increases considerably the total scanning time, particularly in the case of the large dimensions of power electronics (up to 500 mm).

So, we have chosen the following trade-off between probe size, sensitivity and resolution: a probe of 2.5 cm diameter (for a maximal measurement frequency equal to 1 GHz) with a spatial step of 1.25 cm. We proposed to compensate the effects of the probe integration by an image restoration method in order to decrease the equivalent spatial resolution of the field to 2 mm.

2.3. Wiener Filtering

We have adapted the techniques of image restoration in signal processing [7–9] to the improvement of the resolution of data issued from the scanning of the magnetic near-field. In image processing, the different image restoration techniques are: the inverse filtering, the Wiener filtering and the iterative methods. First, we have performed a classical inverse filtering, which isn't presented here. But this technique needs to define an arbitrary cut-off frequency. Then, we have achieved the Wiener filtering, which seemed us easier to complete than the iterative methods and which has already used in electric field measurements [6]. The near-field emission pattern of the probe used is analytically calculated and replaced by an analytical transfer function. The procedure is described and applied next. Let $f(x,y)$ be a H-field strength distribution to be known. The output voltage distribution $g(x,y)$ measured by the H-field probe, whose specification is expressed as its impulse response $t(x,y)$, is described as follows:

$$g(x,y) = t(x,y) * f(x,y) + n(x,y) \tag{6}$$

$*$ is the convolution operator, and $n(x,y)$ is a noise signal.

This relation is more easily described in frequency-domain as a simple product and sum where the capital letters indicate the Fourier transforms of the corresponding spatial functions:

$$G(u,v) = T(u,v) \cdot F(u,v) + N(u,v) \tag{7}$$

u and v are spatial frequencies of x and y quantities. In the field of image processing, $t(x, y)$ is called a point spread function (PSF).

Our goal is to find some function $w(x, y)$ so that we can estimate $f(x, y)$ as follows:

$$\tilde{f}(x, y) = w(x, y) * g(x, y) \tag{8}$$

in such a way that the mean square error is minimised.

The Wiener deconvolution filter provides such a function $w(x, y)$. The filter is more easily described in frequency domain:

$$W(u, v) = \frac{T^*(u, v) S_{ff}(u, v)}{|T(u, v)|^2 S_{ff}(u, v) + S_{nn}(u, v)} \tag{9}$$

$S_{ff}(u, v)$ is the power spectra of the original signal, $S_{nn}(u, v)$ is the power spectra of the noise.

These two terms have a particular importance in the regularization of the Wiener filtering. Unfortunately, there are often unknown. A spread way to get round this consists on considering the signal to noise ratio like a constant.

This transfer function can be also rewritten by:

$$W(u, v) = \frac{1}{T(u, v)} \cdot \frac{|T(u, v)|^2}{|T(u, v)|^2 + K} \tag{10}$$

K is the inverse of the signal-to-noise ratio.

The filtering operation is carried out in the spatial domain:

$$\tilde{F}(u, v) = W(u, v) \bullet G(u, v) \tag{11}$$

Then the inverse Fourier transform is performed on $\tilde{F}(u, v)$ in order to obtain $\tilde{f}(x, y)$.

2.4. Point Spread Function (PSF)

In the aim to apply this technique, it is important to get the PSF $t(x, y)$. In this paragraph, we describe our method. Our first idea was to carry out an experiment with an "hand-made" solenoid. Supposing that this solenoid creates an ideal step-like magnetic field, it leads to the determination of the PSF, called t_{mes}. Next, in order to validate this experiment, we have expressed by formulas the spatial integration of the probe by considering our test conditions: It leads to the calculation of the PSF, called t_{cal}. Then, considering that the magnetic field generated by the solenoid isn't a ideal step function, we have examined the influence of the real magnetic field on the determination of these P.S.F.. Finally, we have searched to obtain a PSF independently of the solenoid radius. This is explained in Paragraph 4.4, and it results in determining the PSF, called t_{th}, which has been compared to the other expressions of the PSF.

In order to simplify the previous formulas, we consider for symmetry reasons, only the variable x. For determining the PSF, we neglect in a first step the noise contribution. Equation (6) can be then written as:

$$g(x) = t(x) * f(x) \tag{12}$$

2.4.1. PSF Obtained by Measurements

We have performed an experiment in a long solenoid for obtaining the PSF, that is $t(x)$; it is shown in Figures 6 and 7. The solenoid parameters are as follows: Radius $R_2 = 20\,\text{mm}$, and length $= 380\,\text{mm}$ and it is consisted of 2000 loops per meter. It is supplied by a sinusoidal voltage (4 Vpp amplitude @ 100 kHz, sine wave).

The solenoid can be assumed as infinitely long (ratiolength/radius ≈ 10), so the magnetic field inside the winding can be considered as constant, its value H_0 is equal to 3.35 A/m. The H-field probe is used to measure the magnetic field inside the solenoid and is moved from the outside (at a distance $x_0 = 48\,\text{mm}$ from the solenoid centre) to the solenoid centre along the x axis (see in Figures 6 and 7). A narrowest slot as possible (4 mm) has been achieved in the solenoid in order to introduce the near field probe. The idea is to consider the magnetic field created by the solenoid as a spatial step distribution $H(x)$, as it is represented ideally in Figure 8 (case (a)).

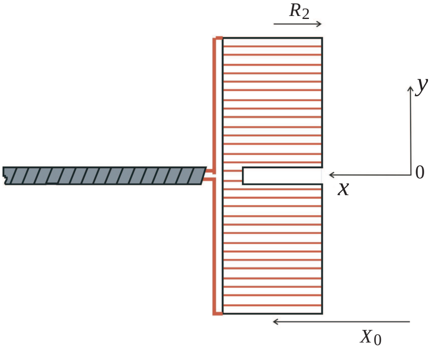

Figure 6. Schema of the solenoid.

Figure 7. Picture of the solenoid.

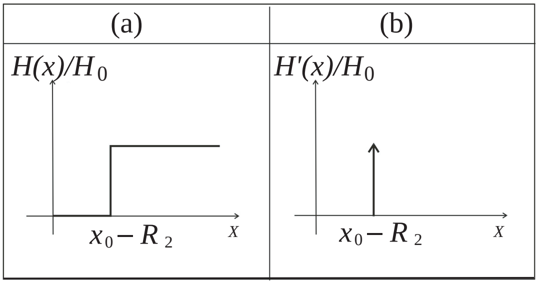

Figure 8. Ideal spatial distribution of the H-field between the inside and the outside of the solenoid.

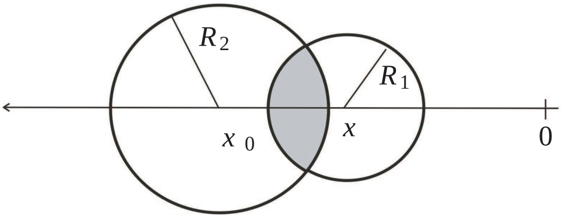

Figure 9. Intersection area of the probe and of the solenoid cross-section.

Based on these assumptions, we can measure and estimate the PSF function $t(x)$ as indicated hereunder: If a Dirac function of H-field $f(x) = \delta(x)$ would be applied to the probe, then its response would be: $g(x) = t(x)$, this response is directly the PSF. Since it's not possible to generate a Dirac function of H-field, we have chosen to create a step function of H-field. If now a step function of H-field is applied to the probe, we deduce that the derivative of $g(x)$ is the PSF: $g'(x) = t(x)$. So, the measurement technique is based on the measurement of the spatial response of the probe and to derive it in order to get the PSF.

From the measured magnetic field $H_m(x)$, the PSF can be expressed by:

$$t_m(x) = \frac{H'_m(x - (x_0 - R_2))}{H_0} \tag{13}$$

2.4.2. PSF Obtained by Calculations

Independently of the technique presented above, it is possible to express the theoretical formulation of the PSF. If we assume that the solenoid is infinitely long, the magnetic field inside is uniform and equals to $H_0 e^{j\omega t}$. We still consider that the magnetic field created by the solenoid is ideal but we search to show the effect of the spatial integration of the probe. Equation (1) becomes:

$$e = -j\omega\mu_0 H_0 A \tag{14}$$

A is the area (represented in Figure 9) of the intersection of two discs of radius R_1 and R_2. The disc of radius R_1 represents the probe area; the disc of radius R_2 represents the solenoid section.

A is expressed by:

$$A(x) = R_1^2 \varphi\left(\frac{-d}{R_1}\right) + R_2^2 \varphi\left(\frac{|x_0 - x| + d}{R_2}\right) \tag{15}$$

if $x_0 \leq x \leq x_0 - (R_1 + R_2)$ and $A(x) = 0$ else with

$$d = \frac{R_2^2 - R_1^2 - |x_0 - x|^2}{2\,|x_0 - x|} \tag{16}$$

and

$$\varphi(f(x)) = \arccos(f(x)) - f(x)\sqrt{1 - (f(x))^2} \tag{17}$$

Then, we can calculate the magnetic field by:

$$H_{cal}(x) = H_0 \frac{A(x)}{\pi R_1^2} \tag{18}$$

We have represented in Figure 10 the measured magnetic field function $H_m(x)$ and the calculated one $H_{cal}(x)$, taking into account the spatial integration. We observe a good agreement between the two last curves ($H_m(x)$ and $H_{cal}(x)$). The observed difference is only due to the assumption that the magnetic field created by the solenoid is a unit step function. The slot, necessary to introduce the near field probe, seems to not affect significantly the measurements.

Nevertheless, in a first approximation, we can consider that the magnetic field created by our solenoid is a spatial step-distribution. Next, we will evaluate the influence of the real field distribution on the P.S.F. determination.

In the same way as previously, the calculated PSF $t_{cal}(x)$ is expressed by:

$$t_{cal}(x) = \frac{H'_{cal}(x - (x_0 - R_2))}{H_0} \tag{19}$$

The function obtained by (13) or (19), can be compared [6] to a Gaussian function, expressed by:

$$t(x) = \frac{c}{\sigma^2} e^{-\frac{x^2}{\sqrt{2}\sigma}} \tag{20}$$

We determine c and σ with the Matlab fminsearch function. As shown by (13) and (19), the measured function $t_m(x)$ and the calculated function $t_{cal}(x)$ have been normalized by dividing by H_0, so that c and σ are independent of the antenna factor and consequently of the frequency. In the case of the measured PSF, we have found $c = 5.8 \times 10^{-7}$ and $\sigma = 11.5 \times 10^{-5}$; in the case of the theoretical calculation, $c = 3.7 \times 10^{-7}$ and $\sigma = 8.14 \times 10^{-5}$. In Figure 11, we have represented the two impulse responses as well as their equivalent

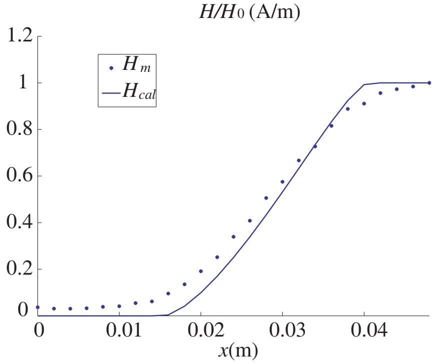

Figure 10. Comparison between the measured magnetic field and the calculated one.

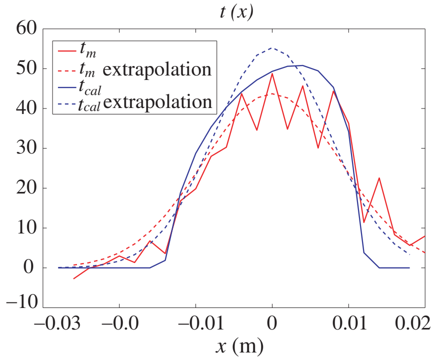

Figure 11. Comparison between the two PSF and their equivalent Gaussian functions.

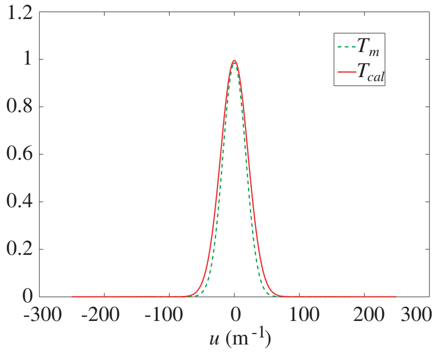

Figure 12. Comparison between the two PSF.

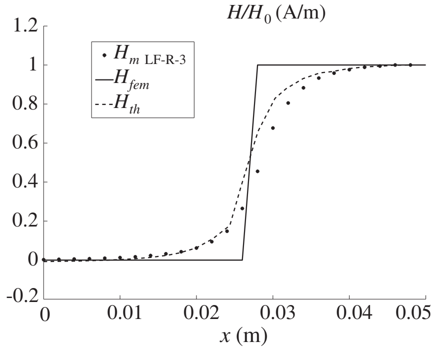

Figure 13. Comparison between the magnetic field obtained by a FEMM freeware and by measurements using 3 mm diameter probe.

Gaussian.

From expression (20), it is easy to calculate the Fourier Transforms, then the PSF is expressed by:

$$T(u) = \frac{c}{\sigma^2}\sqrt{\sqrt{2}\pi\sigma}e^{-\pi^2 u^2 \sqrt{2}\sigma} \tag{21}$$

We have represented in Figure 12 the Fourier Transforms of the two PSF: T_m, with c and σ deduced from measurements and T_{cal} with c and σ deduced from calculations.

We can notice a good agreement between these two curves and conclude that the spatial integration of the probe is correctly taken into account.

2.4.3. Influence of the Real Magnetic Field on the Determination of the P.S.F.

The P.S.F. has been determined by considering the magnetic field created by an ideal solenoid. Yet, the theoretical magnetic field is not the real magnetic field created by the solenoid because it doesn't take into account the effect of the slot. The real magnetic field has been determined either by the finite element method magnetics (FEMM) freeware or by a measurement using a magnetic probe of 3 mm diameter (LF-R-3), in order to eliminate the effect of the spatial integration of the probe. We have represented in Figure 13 the ideal magnetic field function $H_{th}(x)$, the measured one $H_{mLF-R-3}(x)$ and the simulated one $H_{fem}(x)$. Actually, we can notice the effect of the slot on the real magnetic field, which isn't really a unit step function. We can also see a good accordance between the magnetic field measured by the 3 mm-diameter probe and the FEM simulated one. It can be considered that $H_{fem}(x)$ is the real magnetic field.

So in order to evaluate the error made by using (13) to calculate the P.S.F., we have estimated the P.S.F. function $t_r(x)$ directly using (12) with the measured magnetic field $H_m(x)$ as output function and the real magnetic field $H_{fem}(x)$ as input function.

Then, in spatial domain, we can write

$$H_m(x) = t_r(x) * H_{fem}(x) \tag{22}$$

That is, in spatial frequency domain,

$$H_m^f(u) = T_r(u) \cdot H_{fem}^f(u) \tag{23}$$

where $H_m^f(u)$ and $H_{fem}^f(u)$ are the Fourier Transforms of $H_m(x)$ and $H_{fem}(x)$.

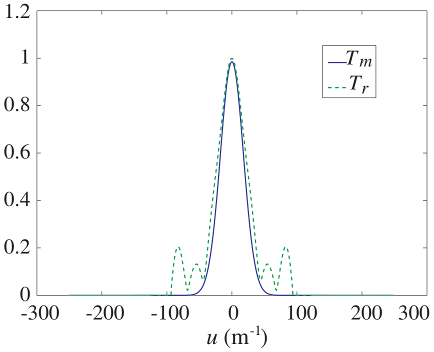

Figure 14. Comparison between the P.S.F. obtained from the real magnetic field and the one obtained with the assumption of an ideal magnetic field.

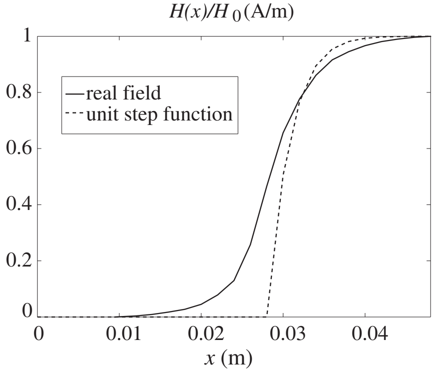

Figure 15. Comparison between the responses of the P.S.F. to the unit step function and to the real magnetic field.

To calculate the discrete Fast Fourier Transform of $H_m(x)$ and $H_{fem}(x)$, we apply the Nicolson ramping algorithm [10]. Then we perform an inverse filtering for determining $T_r(u)$. We had to define a cut-off spatial frequency to avoid the numerical difficulties, encountered when $H^f_{fem}(u)$ is very small. In Figure 14, the obtained P.S.F., $T_r(u)$, is compared to the P.S.F. obtained with the assumption of a step-like function, T_m given by (21) with c and σ deduced from measurements. We can observe a good accordance between the two curves, except for secondary lobes, due to inverse filtering.

To go further, we have calculated the output function $g(x)$ of the Equation (12) with the P.S.F. function $t_m(x)$ given by (13) for an input function $f(x)$ equals successively to a unit step function and to the real magnetic field obtained by the F.E.M. software. In Figure 15, we have represented the response to the unit-step distribution in dash line and the response to the real magnetic field in solid line. The comparison between the two curves is satisfactory: The relative error is about 30% before the point of inflection and 5% after. Because the spatial integration of the probe has been taken into account by the convolution operation, the differences between the two curves are only due to the choice of the input function.

Whatever the method (by inverse filtering with the real magnetic field or by assuming that the magnetic field is a unit step distribution), we can't know precisely the P.S.F. For our application, as we will see in Paragraph 2.5, we have chosen to determine the P.S.F. by assuming that the magnetic field is ideal and by using (13). This method lets us to know the P.S.F. analytically and to avoid performing Fast Fourier Transforms.

2.4.4. Theoretical PSF

We have searched to go further by determining the PSF from the probe dimensional characteristics. As c and σ are independent of the antenna factor, T depends only of the geometric characteristic of the probe. If we put $R_1 = R_2$ in (15), we find:

$$A(x) = R_1^2 \varphi\left(\frac{|x_0 - x|}{2R_1}\right) \tag{24}$$

if $x_0 \leq x \leq x_0 - 2R_1$, and $A(x) = 0$ else, $t_{th}(x)$ is then given by:

$$t_{th}(x) = \frac{A'(x)}{\pi R_1^2} = \frac{2}{\pi R_1}\sqrt{1 - \frac{(x_0 - x)^2}{2R_1}} \tag{25}$$

That is, in the spatial frequency domain:

$$T_{th}(u) = 2\frac{J_1(4\pi u R_1)}{4\pi u R_1} \tag{26}$$

J_1 is the Bessel function of the first kind.

In Figure 16, we have represented the theoretical impulse response, i.e., the PSF. It can be compared to the two curves of Figure 11.

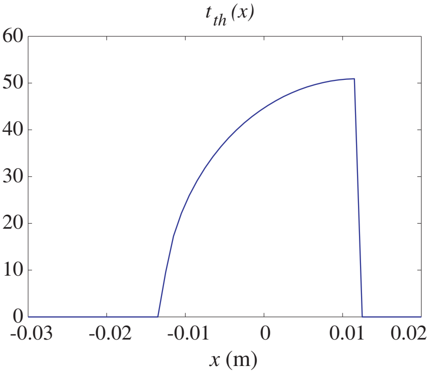

Figure 16. Theoretical PSF.

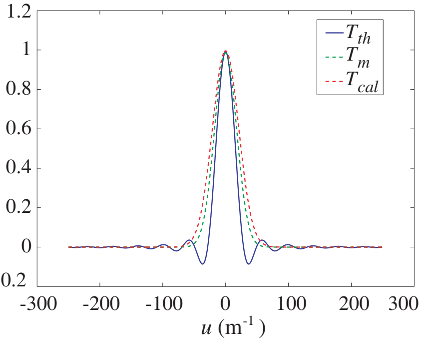

Figure 17. Comparison between the three PSF.

Finally, we have represented in Figure 17, the Fourier Transforms of the three PSF: T_{th}, obtained analytically (25), T_m, given by (13) with c and σ deduced from measurements and T_{cal}, given by (19) with c and σ deduced from calculations.

We can notice a good agreement between these three curves and, in particular, the maxima all equal to 1. T_m and T_{cal} are results of the approximation by a Gaussian whereas T_{th} is a Bessel function. T_{th} shows oscillations and it is stiffer compared to T_m and T_{cal}. In the last paragraph, we will apply the process described in Section 3 by using these three different PSF.

2.5. Concept Validation

2.5.1. Two Dimensions Extension

The previous developments have been presented in 1D with the variable x in order to simplify the problem. In the two dimensions spatial domain (2D), for symmetry reasons, "x" must be replaced by "r", that is "$\sqrt{x^2+y^2}$". This can be translated easily in the frequency domain for the Gaussian expression; by replacing "u" by "ρ", that is "$\sqrt{u^2+v^2}$", (18) can be written by:

$$T(u,v) = \frac{c}{\sigma^2}\sqrt{2}\pi\sigma e^{-\pi^2(u^2+v^2)\sqrt{2}\sigma} \tag{27}$$

Then, the Fourier Transform of the normalized PSF is expressed by:

$$T(u,v) = \frac{c}{\sigma^2}\sqrt{\sqrt{2}\pi\sigma} e^{-\pi^2(u^2+v^2)\sqrt{2}\sigma} \tag{28}$$

As far as the PSF t_{th} is concerned, (25) becomes:

$$t_{th}(x,y) = \frac{2}{\pi R_1}\sqrt{1-\frac{x^2+y^2}{2R_1}} \tag{29}$$

The variable x and y can't be separated and then we can't replace "u" by "$\sqrt{u^2+v^2}$". We have to express t_{th} in polar coordinates, that is,

$$t_{th}(r) = \frac{2}{\pi R_1}\sqrt{1-\frac{r^2}{2R_1}} \tag{30}$$

Then, the Fourier transform can be calculated by:

$$T_{th}(\rho) = 2\pi\int_0^\infty r t_{th}(r) J_0(2\pi\rho r) dr \tag{31}$$

We obtain:

$$T_{th}(\rho) = 16\frac{R_1}{z^2}\left(\frac{\sin z}{z} - \cos z\right) \tag{32}$$

With: $z = 4\pi R_1 \rho$.

The normalized PSF can be expressed by:

$$T_{th}(u, v) = \frac{3}{z^2}\left(\frac{\sin z}{z} - \cos z\right) \tag{33}$$

2.5.2. Application to a Power Transformer

In order to be as clear as possible, we have chosen to show an application of this technique on a simple device, a power electronics transformer, which generates a single radiation frequency. We have measured the z-component of the magnetic field radiated by the transformer shown in Figure 18. Its primary is supplied by a 4 Vpp sinusoidal voltage at 100 kHz, the transformer secondary is open circuit.

We recall that the scan area is in the plane xy and is equal to 110 mm × 110 mm. The measurement has been achieved at a height equal to 74 mm above the ground plane. In accordance with the discussion of Section 2.2, the measurement has been achieved with a 25 mm diameter probe and a step measurement equal to 10 mm. In Figure 19, we present the mapping of the amplitude of the z-component of the magnetic field with a 10 mm step measurement. The measurement time is about 15 minutes. We applied the developed

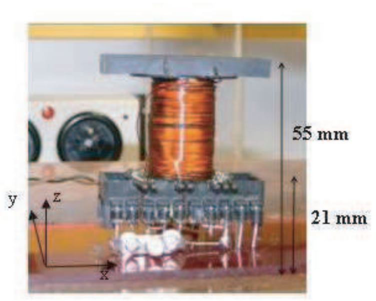

Figure 18. Transformer picture.

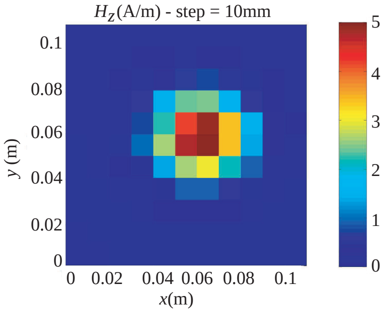

Figure 19. Amplitude of the z-component of the measured magnetic field-step measurement = 10 mm.

technique with the normalized PSF in order to obtain a spatial resolution of 2 mm. Figures 21, 22 and 23 are the mappings obtained by the data post-processing technique. It can be compared with the mapping of Figure 20, which is the measured mapping with a 2 mm measurement step. The measurement time is approximately 6 hours.

We observe a good accordance between the mappings of Figures 21, 22, 23 and 20. This observation can be completed by the curves of the Figure 24. On the Figure 24, we have compared the amplitude of the magnetic field at the cross section $y = 56\,\text{mm}$ obtained by measurements and by reconstruction with Wiener filtering with the Fourier Transform of the three P.S.F.: T_{th}, T_m and T_{cal}. The determination of the P.S.F. by assuming a unit step function (and not the real magnetic field) seems not to affect the obtained mappings.

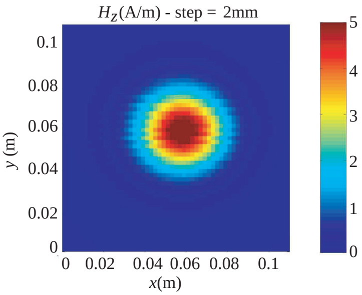

Figure 20. Amplitude of the z-component of the measured magnetic field-step measurement $=$ 2 mm.

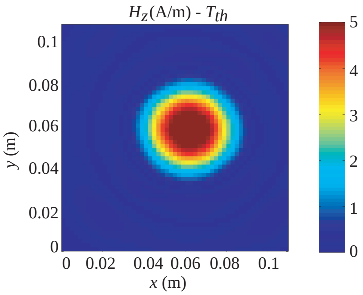

Figure 21. Amplitude of the z-component of the magnetic field deconvoluated by T_{th}.

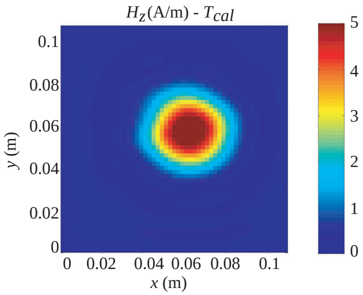

Figure 22. Amplitude of the z-component of the magnetic field deconvoluated by T_{cal}.

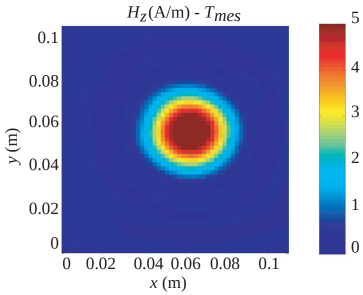

Figure 23. Amplitude of the z-component of the magnetic field deconvoluated by T_m.

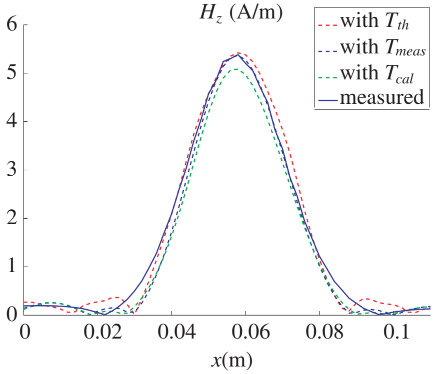

Figure 24. Comparison of the amplitude of the z-component of the magnetic field.

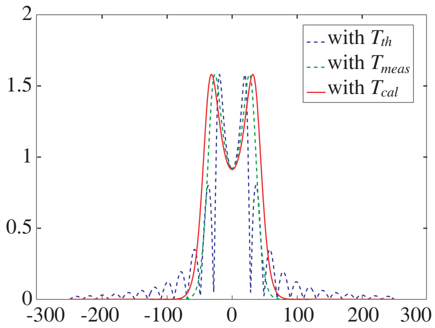

Figure 25. Comparison of the module of $W(u)$.

However, in Figures 21, 22 and 23, we can note some ringings introduced by the data post-processing technique, whatever the used PSF formula. These ringings show the limit of the Wiener filtering, when the measured magnetic field is low and near to noise. Figure 25 represents the module of the transfer function of the Wiener filter, $W(u, v)$, defined by (9) by considering K equal to 0.1 in our case. It confirms that the oscillations are more important with the calculated Fourier Transform PSF T_{cal} rather than with both others. If we increase K, the oscillations decrease but the gain of the filter gets far from 1 and the Wiener filter distorts considerably the signal.

In Figure 20, we can also notice that a well-known mechanical default of our test bench introduces a shift for a measurement step of 2 mm. This problem is drastically reduced by measuring with a larger resolution and applying the data post-processing. We have also to underline the saving of measurement time: It is approximately divided by 25. The Wiener filtering can be applied to near field scannings of more complex EUTs. We have applied it on industrial variable speed drives, which obviously contain many radiating sources in higher frequencies. For these devices, we have to achieve many scannings corresponding to each radiation frequency. The Wiener filtering leads to a very interesting measurement speed reduction and the results are quite satisfactory.

3. CONCLUSION

Magnetic near field scanning have been achieved by a sufficiently large probe to have a good sensitivity and a large measurement step to reduce the test duration. In order to obtain a smaller measurement step, we developed an interpolation technique of the near field scan data. This procedure is based on the Wiener filtering, which supposes the knowledge of the Point Spread Function of the magnetic probe. The P.S.F. of our magnetic probe has been determined by three different ways: two of them are deduced from experiments and the third one is only determined from geometrical characteristics of the magnetic probe. We have tested this technique on the measurements of the amplitude of the magnetic field radiated by a transformer used in power electronics. The experimental results have been compared with the measurements performed with a smaller step. We have observed a good agreement between the results obtained thanks to the different approaches. The interpolation technique described in this paper decreases significantly the measurement step (5×5 times in our experiments) without increasing the test time. However, some ringings have been observed on the results but they appear only with one of the PSF (fully calculated) when the amplitude of the magnetic field is low. This could be improved by using iterative methods like Lucy-Richardson or Van Cittert ones.

REFERENCES

1. Harada, T., N. Masuda, and M. Yamaguchi, "Near-field magnetic measurements and their application to EMC of digital equipment," *IEICE Transactions on Electronics*, Vol. E89-C, 9–15, 2006.
2. Baudry, D., A. Louis, and B. Mazari, "Characterization of the open-ended coaxial probe used for near-field measurements in EMC applications," *Progress In Electromagnetics Research*, PIER 60, 311–333, 2006.
3. Hernando, M., A. Fernandez, F. Arias, F. Rodriguez, and M. Las-Heras, "Radiated noise measurement system to estimate the EMI regulations compliance of a power electronic circuit," *Proc. IEEE International Symposium on Industrial Electronics*, 2544–2549, 2007.
4. Shi, J., M. A. Cracraft, K. Slattery, M. Yamaguchi, and R. E. DuBroff, "Calibration and compensation of near-field scan measurements," *IEEE Transactions on Electromagnetic Compatibility*, Vol. 47, No. 3, 642–650, 2005.

5. Shi, J., R. E. DuBroff, M. Yamaguchi, and K. Slattery, "Frequency domain compensation of probe induced disturbances in near field measurements," *Proc. IEEE Int. Symp. on Electromagnetic Compatibility EMC'04*, 165–168, Sendai, Japan, 2004.
6. Tankielun, A., *Data-post-processing and Hardware Architecture of Electromagnetic Near-field Scanner*, Shaker Verlag, Aachen, 2007.
7. Hirayama, H. and J. Kami, "Resolution improvement of E-field probe using a signal processing technique," *Proc. Korea-Japan AP/EM/EMT Joint Conference*, 206–209, Taejon, Korea, 2001.
8. Gonzales, R. C., *Digital Image Processing*, Addison-Wesley Publishing Company, 1993.
9. Michailovich, O. and A. Tannenbaum, "Blind deconvolution of medical ultrasound images: A parametric inverse filtering approach," *IEEE Transactions on Image Processing*, Vol. 16, No. 12, 3005–3019, 2007.
10. Nicolson, A. M., "Forming the fast Fourier transform of a step response in time-domain metrology," *Electronics Lett.*, Vol. 9, 317–318, 1973.
11. Liu, B., L. Beghou, L. Pichon, and F. Costa, "Adaptive genetic algorithm based source identification with near-field scanning method," *Progress In Electromagnetics Research B*, Vol. 9, 215–230, 2008.
12. Ayestaran, R. G. and F. Las-Heras, "Near field to far field transformation using neural networks and source reconstruction," *Journal of Electromagnetic Waves and Applications*, Vol. 20, No. 15, 2201–2213, 2006.